SPECIAL
International Symposium on Tropospheric Profiling
COLLECTION

Evaluation of an LES-Based Wind Profiler Simulator for Observations of a Daytime Atmospheric Convective Boundary Layer

DANNY E. SCIPIÓN

School of Electrical and Computer Engineering, and Atmospheric Radar Research Center, University of Oklahoma, Norman, Oklahoma

PHILLIP B. CHILSON

School of Meteorology, and Atmospheric Radar Research Center, University of Oklahoma, Norman, Oklahoma

EVGENI FEDOROVICH AND ROBERT D. PALMER

School of Meteorology, University of Oklahoma, Norman, Oklahoma

(Manuscript received 9 January 2007, in final form 13 November 2007)

ABSTRACT

The daytime atmospheric convective boundary layer (CBL) is characterized by strong turbulence that is primarily caused by buoyancy forced from the heated underlying surface. The present study considers a combination of a virtual radar and large eddy simulation (LES) techniques to characterize the CBL. Data representative of a daytime CBL with wind shear were generated by LES and used in the virtual boundary layer radar (BLR) with both vertical and multiple off-vertical beams and frequencies. To evaluate the virtual radar, a multiple radar experiment (MRE) was conducted using five virtual radars with common resolution volumes at two different altitudes. Three-dimensional wind fields were retrieved from the virtual radar data and compared with the LES output. It is shown that data produced from the virtual BLR are representative of what one expects to retrieve using a real BLR and the measured wind fields match those of the LES. Additionally, results from a frequency domain interferometry (FDI) comparison are presented, with the ultimate goal of enhancing the resolution of conventional radar measurements. The virtual BLR produces measurements consistent with the LES data fields and provides a suitable platform for validating radar signal processing algorithms.

1. Introduction

Turbulence in the daytime atmospheric convective boundary layer (CBL) is primarily forced by heating of the surface, radiational cooling from clouds at the CBL top, or by both mechanisms. The CBL is considered clear when no clouds are present (Holtslag and Duynkerke 1998), as in this study. In this case, the main forcing mechanism in the CBL is heating of the surface.

Turbulent convective motions in the CBL transport the heat upward in the form of convective plumes or thermals. These rising motions and associated downdrafts effectively mix momentum and potential temperature fields in the middle portion of the CBL (Zilitinkevich 1991). The resulting mixed layer is typically the thickest sublayer within the CBL. The CBL is topped by the entrainment zone, which has relatively large vertical gradients of averaged (in time or over horizontal planes) meteorological fields. The entrainment zone is often called the interfacial or capping inversion layer because it is collocated with the region of maximum gradients in the potential temperature profile. The height of the capping inversion is usually denoted by z_i. A pure buoyancy-driven CBL rarely exists, and there are many situations in which the surface heating is relatively weak while the production of turbulence by wind shears is relatively strong. In these

Corresponding author address: Danny E. Scipión, University of Oklahoma, School of Meteorology, 120 David L. Boren Blvd., Room 5900, Norman, OK 73072-7307.
E-mail: dscipion@ou.edu

DOI: 10.1175/2007JTECHA970.1

cases, the shear effects on the CBL turbulence dynamics cannot be ignored (Conzemius and Fedorovich 2006).

A widely used instrument for the study and monitoring of the lower atmosphere is the boundary layer radar (BLR). The term BLR is generally applied to a class of pulsed Doppler radar that transmits radio waves vertically, or nearly vertically, and receives Bragg backscattered signals from refractive index fluctuations of the optically clear atmosphere. The operating frequency of this type of radar is typically near 1 GHz. Therefore, the Bragg scale is such that BLRs are sensitive to turbulent structures that have spatial scales near 15 cm. Enhanced refractive index variations are often associated with the entrainment zone just above the CBL, which can be detected by clear-air radar. There have been many studies in which BLRs are used to estimate the height of the atmospheric boundary layer (ABL) and thickness of the entrainment layer (e.g., Angevine et al. 1994; Angevine 1999; Cohn and Angevine 2000; Grimsdell and Angevine 2002). Profiles of the wind vector directly above the instrument are obtained using the Doppler beam swinging (DBS) method (Balsley and Gage 1982). BLRs are also sensitive to Rayleigh scatter from hydrometeors and are used to study clouds and precipitation (Gage et al. 1994; Ecklund et al. 1995). Thus, the BLR can be used to study the boundary layer under a wide variety of meteorological conditions and has proven invaluable for such investigations (e.g., Rogers et al. 1993; Angevine et al. 1994; Wilczak et al. 1996; Dabberdt et al. 2004).

Frequency-modulated continuous-wave (FMCW) radar measurements have been used to show that the thermodynamic fields within the CBL can exhibit a high degree of complexity and that organized finescale structures with spatial scales of roughly 1 m are common (Eaton et al. 1995). Unfortunately, BLRs must operate within stringent frequency management constraints, which limit their range resolution. A typical range resolution for BLR measurements of the ABL is about 100 m, which is too coarse to adequately reproduce the spatial structure embedded within the entrainment zone. Several multiple-radar-frequency techniques have been introduced in the past as a means of improving the range resolution (Kudeki and Stitt 1987; Palmer et al. 1990, 1999; Luce et al. 2001). Multiple-frequency techniques have been successfully used to study the ABL at UHF (Chilson et al. 2003; Chilson 2004).

Complementary to field observations of the CBL by in situ and remote sensing measurement methods, numerical simulation approaches—specifically, the large eddy simulation (LES) technique—are widely employed to study physical processes in the atmospheric CBL. Large eddy simulations of CBL-type flows have become a routine scientific exercise over the last three decades (see, e.g., Deardorff 1972; Moeng 1984; Mason 1989; Schmidt and Schumann 1989; Moeng and Sullivan 1994; Sorbjan 1996, 2004; Khanna and Brasseur 1998; Sullivan et al. 1998; vanZanten et al. 1999; Fedorovich et al. 2001, 2004b; Conzemius and Fedorovich 2006). All of these cited works are indicative of LES gradually becoming an applied research technique in CBL studies. Nonetheless, the relation of LES to observations of the CBL, as well as to conceptual CBL models or theories, needs further examination and quantitative evaluation (Wyngaard 1998; Stevens and Lenschow 2001).

The LES method is based on the numerical integration of filtered equations of flow dynamics and thermodynamics that resolve most of the energy-containing scales of turbulent transport. Any motions that are not resolvable are assumed to carry only a small fraction of the total energy of the flow and are parameterized with a subgrid (or subfilter) closure scheme. In the LES of the atmospheric CBL, the environmental parameters such as surface heating, stratification, and shear can be precisely controlled. Retrieval of spatial turbulence statistics in LES does not necessarily rely on additional assumptions like the Taylor (1938) frozen turbulence hypothesis: thermodynamic and kinematic properties of the simulated flow are known at all points of the numerical grid simultaneously. In this manner, LES has been a helpful tool for studying the statistics of (resolved) CBL turbulence and for visualizing the turbulence structure of the CBL; however, the applicability of LES in atmospheric boundary layer studies is limited by the ability of the subgrid model to adequately describe the effects of the subgrid motions on the filtered (resolved) fields. This is the price that must be paid to simulate turbulence in larger domains with heterogeneous turbulence properties. Also, like all numerical approaches based on temporal and spatial discretization of the governing flow equations, LES is subject to various numerical artifacts, including phase speed errors, artificial viscosity, and dispersion errors.

One method of incorporating LES data into the study of the ABL is through the creation of a virtual BLR; that is, simulated radar time series signals can be generated based on the characteristics of the LES fields (Muschinski et al. 1999, hereafter MSW99). Here, the term "time series data" is used to indicate the time histories of discretely sampled complex radar voltages (in-phase and quadrature) corresponding to a backscat-

tered signal. First, a field of refractive index C_n^2 is calculated from the LES output using computed values of pressure, potential temperature, and specific humidity. The Bragg scattering amplitude is then related to the calculated values of C_n^2, and the phases are computed using the LES velocity components at each LES time step using the local and instantaneous version of Taylor's (1938) frozen turbulence hypothesis. The amplitude and phases are then interpolated in time between the consecutive LES time steps (1-s separation). Radar time series are compiled by summing the contribution from each point within the radar resolution volume, which is determined by the radar pulse and beamwidth.

In this study we present a virtual BLR, which is based on the work of MSW99. The differences between our virtual radar and the one developed by MSW99 are the flexibility of multiple beams (vertical and off-vertical), made possible though the calculation of oblique C_n^2 at each grid point; the interpolation of the C_n^2 and velocity at each time step of the virtual BLR; the addition of noise after the time series data are generated; and simulation of multiple frequencies. The virtual BLR output data are then employed to estimate CBL characteristics, like the three-dimensional wind fields and C_n^2, which are compared to the "ground truth" (reference) LES data.

The paper is organized as follows: in section 2, the large eddy simulation is presented, as well as a description of how the structure function parameter of refractivity C_n^2 is calculated over an oblique position. The radar simulator is described in section 3. Section 4 shows the results of the many tests committed with the virtual BLR, including the spectral analysis of the signal, the multiple radar experiment (MRE), and the frequency domain interferometry (FDI) implementation. Conclusions and future work are discussed in section 5.

2. Numerical data generator

Time series data for the virtual BLR presented here are generated following the approach developed in MSW99. The virtual BLR ingests outputs of LES of a clear CBL, which has been extensively tested in comparison with several other representative LES codes and against experimental data for clear CBLs with and without shear, and has been found to confidently reproduce turbulence structure for a broad variety of flow regimes observed in the clear CBL (Fedorovich et al. 2004a). On the other hand, LES of cloud-topped and, especially, stable boundary layers is associated with a number of conceptual and numerical complications, and the reliability of the LES-generated turbulence fields for these layer types is not as established as for the clear CBL. This makes the clear CBL case ideal for our study.

The virtual BLR is based on an LES code that was developed along the lines described in Nieuwstadt (1990) and Fedorovich et al. (2001, 2004a). With respect to many of its features, the code was specifically designed to simulate CBL-type flows characterized by the presence of large-scale turbulent structures transporting the dominant portion of the kinetic and thermal energy of the flow. Fields of atmospheric parameters generated by LES are used as input fields for the BLR simulator. The code was extensively tested in comparison with several other representative LES codes and against experimental data for clear CBLs with and without wind shear (Fedorovich et al. 2004a); it was found to confidently reproduce turbulence structure for a broad variety of flow regimes observed in the clear CBL.

The simulation run for the present study was performed in a rectangular domain composed of 10-m grid cells. The domain size is given by $X \times Y \times Z = 2000\ \text{m} \times 2000\ \text{m} \times 2000\ \text{m}$. Correspondingly, there are $200 \times 200 \times 200$ grid points. The time discretization is 1 s. The following external parameters were assigned during the run: the free-atmosphere horizontal wind was set to 5 m s^{-1} in the x direction and 0 m s^{-1} in the y direction; the free-atmosphere potential temperature gradient was 0.004 K m^{-1}; and the surface kinematic heat flux, surface kinematic moisture flux, and surface roughness length were 0.2 K m s^{-1}, 10^{-4} m s^{-1}, and 0.01 m, respectively.

A subset of the LES output was used for the radar simulator. The subdomain size is given by $750\ \text{m} \leq x \leq 1250\ \text{m}$, $750\ \text{m} \leq y \leq 1250\ \text{m}$, and $200\ \text{m} \leq z \leq 1200\ \text{m}$. The output included resolved (in the LES sense) three-dimensional fields of potential temperature Θ; specific humidity q; flow velocity components u, v, and w; and subgrid turbulent kinetic energy E, as presented in Fig. 1 and summarized in Table 1. [See Conzemius and Fedorovich (2006) for additional information about the numerical setup.]

According to the radar equation, the backscattered signal power from a collection of distributed targets is directly proportional to the radar reflectivity η. The value of η represents the cumulative effect of the radar cross sections for the individual targets. For the case of scatter resulting from turbulent variations in the refractive index (clear-air scatter), the echo power is also related to the radar reflectivity; however, η is now given by the well-established theoretical relationship

$$\eta = 0.379 C_n^2 \lambda^{-1/3}, \tag{1}$$

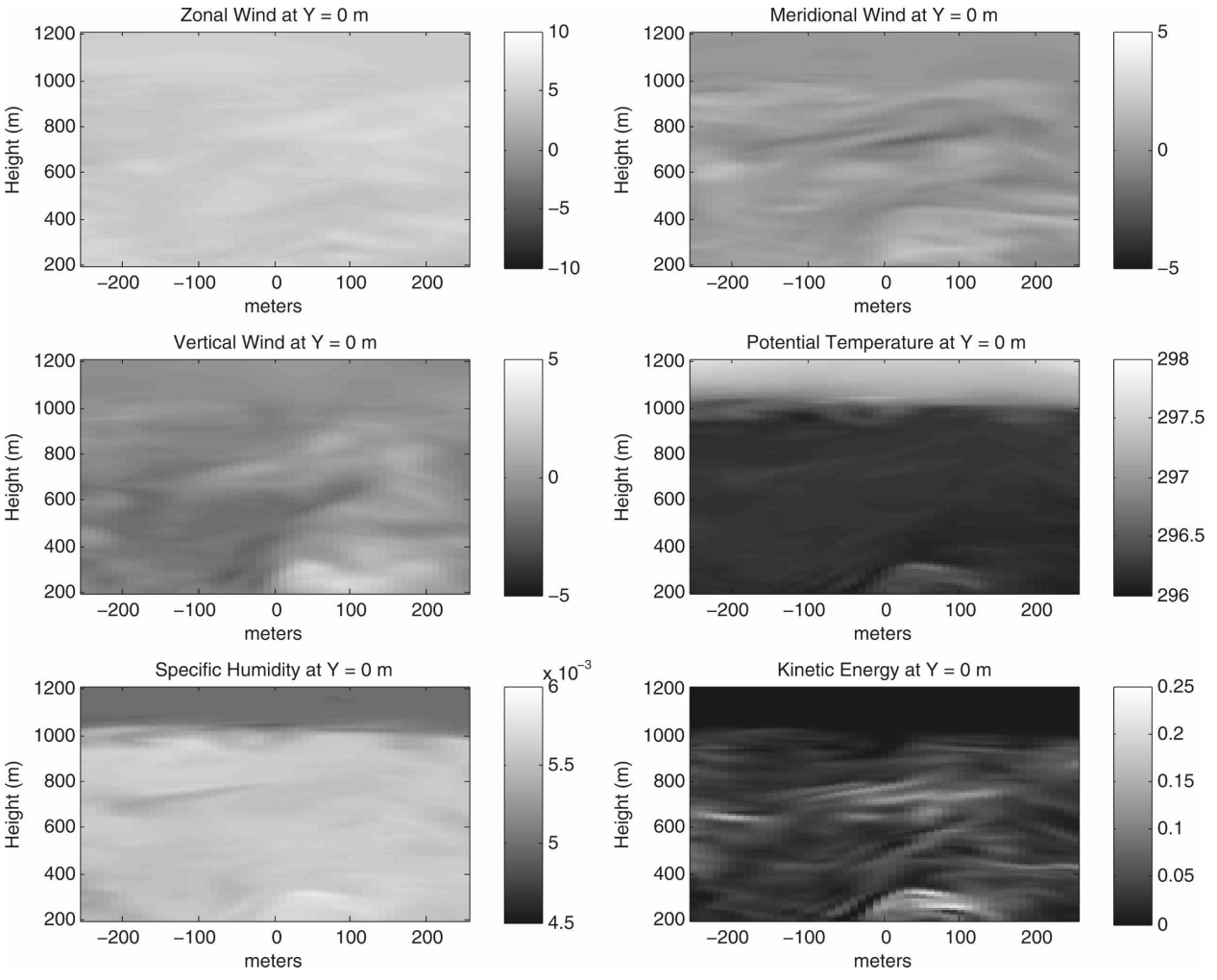

FIG. 1. Examples of LES output fields in the subdomain of the radar simulator. (top left) Zonal wind, (top right) meridional wind, (center left) vertical velocity, (center right) potential temperature, (bottom left) specific humidity, and (bottom right) subgrid kinetic energy. All data refer to the same single realization in time (one LES time step).

where C_n^2 is the structure function parameter of the refractive index and λ is the radar wavelength (Tatarskii 1961; Ottersten 1969). It is assumed that the turbulence is isotropic and in the inertial subrange. Further, the radar resolution volume is assumed to be uniformly filled with turbulence.

TABLE 1. Description of the LES subdomain used by the radar simulator.

Property	Specification
No. of grid points	$51 \times 51 \times 101$
Spatial resolution	10 m
Time step	1 s
Subdomain dimensions	500 m $\times$ 500 m $\times$ 1000 m
Variables	u, v, w, E, q, Θ

The structure function parameter of refractivity C_n^2 is by definition derived from the refractive index field using

$$C_n^2 = \frac{\langle [n(\mathbf{r} + \boldsymbol{\delta}) - n(\mathbf{r})]^2 \rangle_r}{|\boldsymbol{\delta}|^{2/3}}, \tag{2}$$

where n is the refractive index and $\langle\ \rangle_r$, as mentioned in MSW99, denotes the spatial average over a volume within which the n irregularities are assumed to be statistically isotropic and homogeneous. Here, $\mathbf{r}$ represents the position vector and $\boldsymbol{\delta}$ is the vector defining the spatial separation. The refractive index is related to the refractivity N through $n = 1 + N \times 10^{-6}$. If we assume that the background atmospheric pressure profile is hydrostatic, then the refractivity is found directly from the

simulation output parameters through the following equations (Bean and Dutton 1966; Holton 2004):

$$N = \frac{77.6}{T}\left(P + 4811\frac{e}{T}\right), \tag{3}$$

$$d\ln P = -\frac{g}{RT}dz, \tag{4}$$

$$T = \Theta\left(\frac{P}{P_0}\right)^{0.286}, \quad \text{and} \tag{5}$$

$$e = \frac{qP}{0.622 + q}, \tag{6}$$

where P is the atmospheric pressure (hPa), $e(q, T)$ is the partial pressure of water vapor (hPa), P_0 represents the pressure at $z = 0$ m (1000 hPa), g is the gravitational acceleration (9.81 m s^{-1}), R is the gas constant for dry air (287 J kg^{-1} K^{-1}), and T is the absolute temperature (K).

To calculate C_n^2 within each grid cell of the LES domain, Eq. (2) was applied along a line (beam) connecting the position of the virtual radar and the center of the grid cell, where C_n^2 needed to be estimated (Fig. 2, left-hand side). However, the scale δ (magnitude of $\boldsymbol{\delta}$) to be considered corresponds to the Bragg scale ($\delta = \lambda/2$) for which the radar is sensitive. This Bragg scale (~16 cm for a frequency of 915 MHz) is much smaller than the LES grid cell size ($\Delta \sim 10$ m). Therefore, Eq. (2) must be scaled as shown below:

$$C_n^2 = \frac{(\Delta n')^2}{\delta^{2/3}}, \tag{7}$$

$$\frac{\Delta n'}{\delta} = \frac{\Delta n}{\Delta}, \quad \text{and} \tag{8}$$

$$C_n^2 = \frac{\left(\frac{\Delta n}{\Delta}\delta\right)^2}{\delta^{2/3}}, \tag{9}$$

where $\Delta n'$ represents the gradient of the refractive index n at the Bragg scale (which is considered to be isotropic on the scales sensed by the radar), Δn represents the gradient of the refractive index at the grid scale, and Δ represents the oblique distance between the layers where the Δn is estimated. Although the gradient of the grid spacing is assumed to be the same at the Bragg scale, C_n^2 must be rescaled to account for the nonlinear functionality of the $|\boldsymbol{\delta}|^{2/3}$ term in the gradient of Eq. (2).

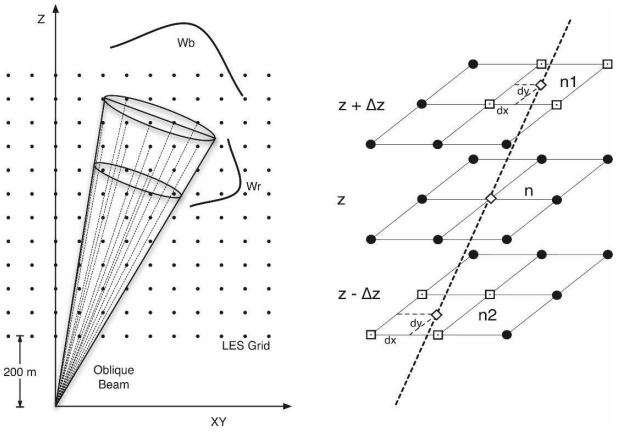

FIG. 2. (left) Scheme representing an off-vertical pointing beam. The dotted lines represent the distance from the location of the radar to the grid points of the LES within the resolution volume. Along these dotted lines, C_n^2 is calculated and later weighted in range (W_r) and beamwidth (W_b). (right) The dotted line represents the axis along which C_n^2 needs to be estimated. First, the value of n at level z is obtained from the LES matrix; however, at levels $z + \Delta z$ and $z - \Delta z$ the dotted line does not match any of the LES grid points. To obtain an estimate at those heights, a linear interpolation is made using the four closest points. Finally, an average of the two gradients of n (from z and $z + \Delta z$, and z and $z - \Delta z$) is computed.

To estimate Δn, the refractive index n was calculated in the center of the grid cell at a level z with respect to the ground and at two levels displaced from z in height by an increment Δz (Fig. 2, right-hand side); that is, the points at z, $z - \Delta z$, and $z + \Delta z$ are considered. A bilinear interpolation was then applied to obtain an estimate of n between the closest four points on the upper and lower planes, thereby calculating values of n along the beam as follows:

$$n_{xy} = (1 - dx)(1 - dy)n_{x0y0} + (dx)(1 - dy)n_{x1y0} + (1 - dx)(dy)n_{x0y1} + (dx)(dy)n_{x1y1}, \quad \text{and}$$

$$dx = \frac{x - x_0}{x_1 - x_0}, \quad dy = \frac{y - y_0}{y_1 - y_0}, \tag{10}$$

where n_{xy} represents the refractive index n at point (x, y), which does not match any of the grid points, and n_{xiyj} denotes refractive index values at x_i, y_j; $i, j = 0, 1$.

This modification, along with the average over two consecutive layers, constitutes a significant refinement from the work of MSW99; it yields

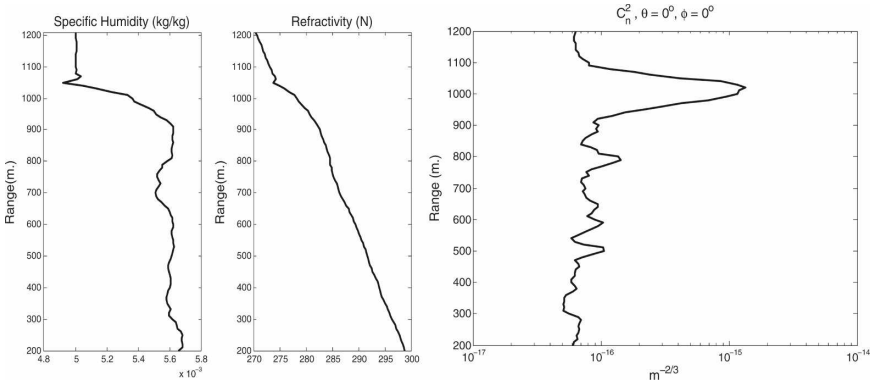

FIG. 3. Vertical profiles of (left) specific humidity characteristic for the CBL, (center) the refractivity calculated from the LES fields, and (right) the horizontally averaged structure function parameter of refractivity C_n^2. All data were calculated from a single realization in time.

$$C_n^2(x, y, z, t) = \frac{1}{2}\left[\frac{\left(\frac{n_1 - n}{\Delta}\delta\right)^2}{\delta^{2/3}} + \frac{\left(\frac{n - n_2}{\Delta}\delta\right)^2}{\delta^{2/3}}\right], \tag{11}$$

where n_1, n, and n_2 represent the refractive index at levels $z + \Delta z$, z, and $z - \Delta z$, respectively, as depicted in the right-hand side of Fig. 2. A sample vertical profile of the specific humidity q from the LES output, the corresponding calculated profiles of refractivity N, and the horizontal averaged structure function parameter of refractivity C_n^2 are presented in Fig. 3 for a single realization in time.

3. Radar simulator

Various approaches to generating time series data for radar simulations can be found in the literature. One that was studied by Sheppard and Larsen (1992), Holdsworth and Reid (1995), Yu (2000), and Cheong et al. (2004) consists of creating a *sampling domain* populated with scattering points. These points move within the domain according to the field of instantaneous wind vector. Another method considers the grid cells of the model as a scattering center, and the phase of the radar signal from the scattering center is modulated by the local instantaneous velocity field (MSW99). Therefore, by varying the phase, without actually moving the scatterer, the expected Doppler velocity can be generated. Some implementation advantages exist with such a method, especially with regard to scatterer position update.

The radar simulator for this study was developed following the Eulerian frame approach of MSW99. The signal amplitude in the simulator after time τ is proportional to C_n^2 and inversely proportional to r_0^2, which is the range of the center of the sampling volume. The phase difference is proportional to the velocity vector as follows:

$$V(t_0 + \tau) = A' \sum_{p=1}^{N} \sqrt{C_n^2(t_0 + \tau)^{(p)} W_r^{(p)} W_b^{(p)}} \times \exp\left[-j(\varphi_0^{(p)} + k_B r^{(p)} + \mathbf{k}_B^{(p)} \cdot \mathbf{v}^{(p)}(t_0 + \tau)\tau)\right], \quad \text{and}$$

$$A' = \frac{G}{\lambda r_0^2}\sqrt{0.0330}\, k_B^{-11/6}, \tag{12}$$

where p represents each individual grid point of the N points contained within the resolution volume; G is a constant proportional to the power transmitted and the gain of the transmitter and receiver; $\varphi_0^{(p)}$ is a random initial phase; k_B is the Bragg wavenumber [$k_B = (4\pi/\lambda)$]; $\mathbf{k}_B^{(p)}$ is the Bragg wave vector that is directed from the center of the antenna to the center of the pth LES grid cell and has the magnitude of k_B; $r^{(p)}$ is the distance from the center of the antenna to the center of the cell; and $\mathbf{v}^{(p)}$ is the instantaneous radial velocity. In addition, W_r represents the range-weighting function and is described by Holdsworth and Reid (1995) as

$$W_r(x, y, z) = \exp\left[\frac{(r - r_0)^2}{2\sigma_r^2}\right], \tag{13}$$

where r represents the projection of the range of each grid point ($\sqrt{x^2 + y^2 + z^2}$) over the pointing direction; r_0 is the range of the center of the scattered volume; and the variance $\sigma_r = 0.35c\tau_p/2$, where c is the speed of light and τ_p is the pulse width (Doviak and Zrnić 1993). Finally, the beam-pattern weighting function (W_b) is defined by the following equation (Yu 2000; Cheong et al. 2004):

$$W_b(x, y, z) = \exp\left[-\frac{(\theta_x - \overline{\theta_x})^2}{2\sigma_x^2} - \frac{(\theta_y - \overline{\theta_y})^2}{2\sigma_y^2} \right], \quad \text{and} \quad \theta_x = \tan^{-1}\left(\frac{x}{z}\right), \theta_y = \tan^{-1}\left(\frac{y}{z}\right), \tag{14}$$

where $\overline{\theta_x}$ and $\overline{\theta_x}$ describe the antenna beam pointing in degrees and $\sigma_x = \sigma_y = \theta_1/2.36$ are proportional to the beamwidth (θ_1) in degrees. Significant improvements on the work presented by MSW99 include the following: (i) the values of C_n^2, which are calculated over oblique beams along the radial, and the velocity are now interpolated at each time τ, and (ii) a range term $[k_B r^{(p)}]$, which is important for further multiple frequencies applications such as FDI, is now incorporated in the phase term.

Because the LES generates data for variables at a time step of 1 s and the radar interpulse period (IPP) is on the order of milliseconds, an estimation of any of the variables X at $t_0 + \tau$ is needed. To achieve this, the desired value is calculated using a linear interpolation scheme presented by Cheong et al. (2004):

$$X(t_0 + \tau) = (1 - \tau)X(t_0) + \tau X(t_1), \tag{15}$$

where t_0 and t_1 are two consecutive time steps of the LES and τ is the intermediate value taken from 0 to 1. Also, assume that $\text{var}[X(t_0)] = \text{var}[X(t_1)] = \text{var}(X)$, where var() denotes the variance. Thus, the variance of the interpolated random variable $X(t_0 + \tau)$ is given by

$$\text{var}[X(t_0 + \tau)] = [(1 - \tau)^2 + 2\rho(1 - \tau)\tau + \tau^2]\,\text{var}(X), \tag{16}$$

which causes $\text{var}[X(t_0 + \tau)]$ to be reduced in a quadratic form as a function of τ, as shown in the previous equation. To reverse this artifact, the interpolated value can be scaled with the inverse square root function of the equation. Therefore, the scaled interpolated value is

$$f_i'(x) = \frac{1}{\sqrt{(1 - \tau)^2 + 2\rho(1 - \tau)\tau + \tau^2}} f_i(x), \tag{17}$$

where ρ is the cross-correlation factor of $X(t_0)$ and $X(t_1)$.

a. Radar setup

The virtual radar in this study is patterned after a Vaisala UHF BLR (LAP3000) operating at a central frequency of 915 MHz, with a half-power beamwidth of 9°. It is possible to direct the radar beam vertically or electronically steered at 23° off-vertical along four different azimuth angles: 0°, 90°, 180°, and 270°. In the present study, different off-vertical positions and range resolutions were chosen to validate the virtual BLR. The parameters chosen for the virtual BLR are presented in Table 2.

To produce realistic results from the virtual UHF BLR, it is necessary to introduce additive white noise to our generated time series data. First, the maximum power of the signal is estimated from the time series data; then, the variance of the background is computed based on a desired signal-to-noise ratio (SNR). The complex white noise is generated based on the assumption that it has a Gaussian distribution described by the previously calculated variance. This procedure is independently applied to the real and imaginary components of the time series data. The complex Gaussian noise is simply added to the original time series data. An example of time series data corresponding to a vertically pointing beam is presented in Fig. 4. The additive complex Gaussian noise shown was calculated for an SNR of 10 dB.

b. Spectral analysis

A conventional spectral processing procedure was used to calculate the Doppler moments from the resulting complex time series data (including the additive noise). First, the Doppler spectra were found and then the noise level was estimated using the algorithm described in Hildebrand and Sekhon (1974). After the spectral levels were reduced to compensate for the estimated noise level, the first three moments (power, mean radial velocity, and spectrum width) were estimated following Doviak and Zrnić (1993).

An example of the spectral analysis is provided in Fig. 5 for a virtual radar located at $x = 130$ m, $y = -130$ m, and $z = 0$ m with respect to the center of the LES volume. The simulated radar beam has a width of 9° and is directed northwest at 10° off-vertical. The range resolution was 50 m. Overall, the results shown in each of the panels in Fig. 5 compare well with actual

TABLE 2. Virtual BLR specifications.

Quantity	Value
Frequency	915 MHz
Wavelength	32.8 m
Full half-power beamwidth	9°
Interpulse period	5 ms
Resolution	50 m
Beam inclination	Variable

BLR data. Comparing the mean radial velocities estimated from the virtual BLR and the simulated truth from the LES (single profile pointing to the same direction), it can be seen that there is good agreement between the two datasets. Some differences are to be expected simply because of the disparate sizes of the sampling volumes resulting from a measurement along a single radial versus a 9° beamwidth. Although not shown here, additional radar simulator results were generated using a narrower beamwidth. Not surprisingly, the agreement between the estimated radial velocity and the simulated truth from the LES was improved for this case.

We now consider the estimated signal power from the radar simulator. Figure 5 (center right) shows the range-corrected power from the virtual BLR and the beam-weighted $C_n^2(W_bC_n^2)$ obtained from the LES. The maximum of the range-corrected power represents the top of the CBL, also known as the inversion layer, and its evolution over 10 min of the simulation period can be observed in the bottom panel. Again, there exists a marked agreement between the simulated radar and LES fields.

4. Sample applications of the LES-based radar simulator

Here we present two sample applications of the radar simulator. These have been primarily designed as a means of testing and validation. One is a simulated multiple radar experiment in which five virtual radars are used to simultaneously probe a common volume within the LES domain. The second is a multiple frequency experiment meant to test the suitability of the simulated time series data for the range-enhancing algorithms discussed earlier.

a. Multiple radar experiment

For the multiple radar experiment, the virtual radars were located approximately equidistant from one another as illustrated in Fig. 6. The center radar within the LES domain used a vertically oriented beam. The other

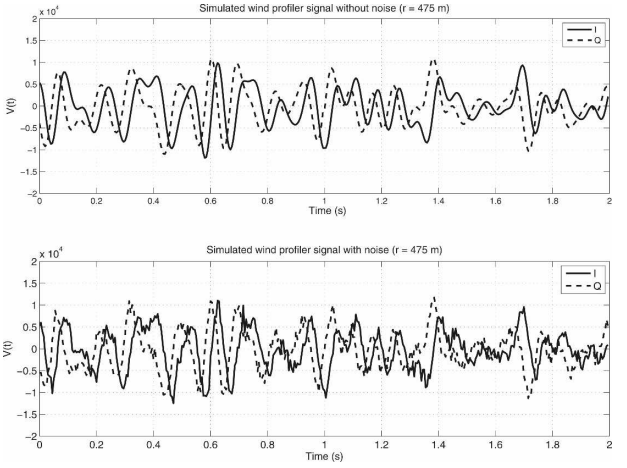

FIG. 4. Time series data from the simulated BLR data $V(t)$ obtained at a range of 475 m, (top) without and (bottom) with additive Gaussian noise (SNR = 10 dB). The solid line represents the real part (in phase) of $V(t)$ and the dotted line is the imaginary part (quadrature) of $V(t)$.

four radars had beams that were directed off-vertical but pointed toward the vertical beam of the first radar. The net effect is two distinct sampling volumes.

For this experiment, C_n^2 was calculated for the five different positions following the criteria described in section 2. The radar simulation time corresponds to 5 and 10 min for the ~500- and ~1050-m cases, respectively. The specific parameters for the experiment setup are shown in Table 3.

The nine radar beams simulated for the experiment were divided in two groups. The first group (A, B, C, D, and E) and second group (A′, B′, C′, D′, and E) correspond to the ~500- and ~1050-m cases, respectively. Each group of five radars was directed toward the same resolution volume. Because the power of the BLR is proportional to C_n^2, and it is not aspect sensitive, the range-corrected power estimates at any height are expected to be the same. As observed in Fig. 7, which corresponds to the first group, the power levels are indeed similar. When analyzing the ~1050-m case (Fig. 8), there is good agreement between the range-corrected power of all the oblique radars, but a noticeable bias exists for the vertically pointing radar. This is caused by a volume mismatch between the vertical and the oblique radar beams.

Another procedure to validate the virtual radars is to compare the retrieved wind velocity vector from the virtual BLR and the truth from the LES. The mean radial velocity for the five radars was estimated following the procedure described in section 3. The radial velocity is a function of the three-dimensional wind

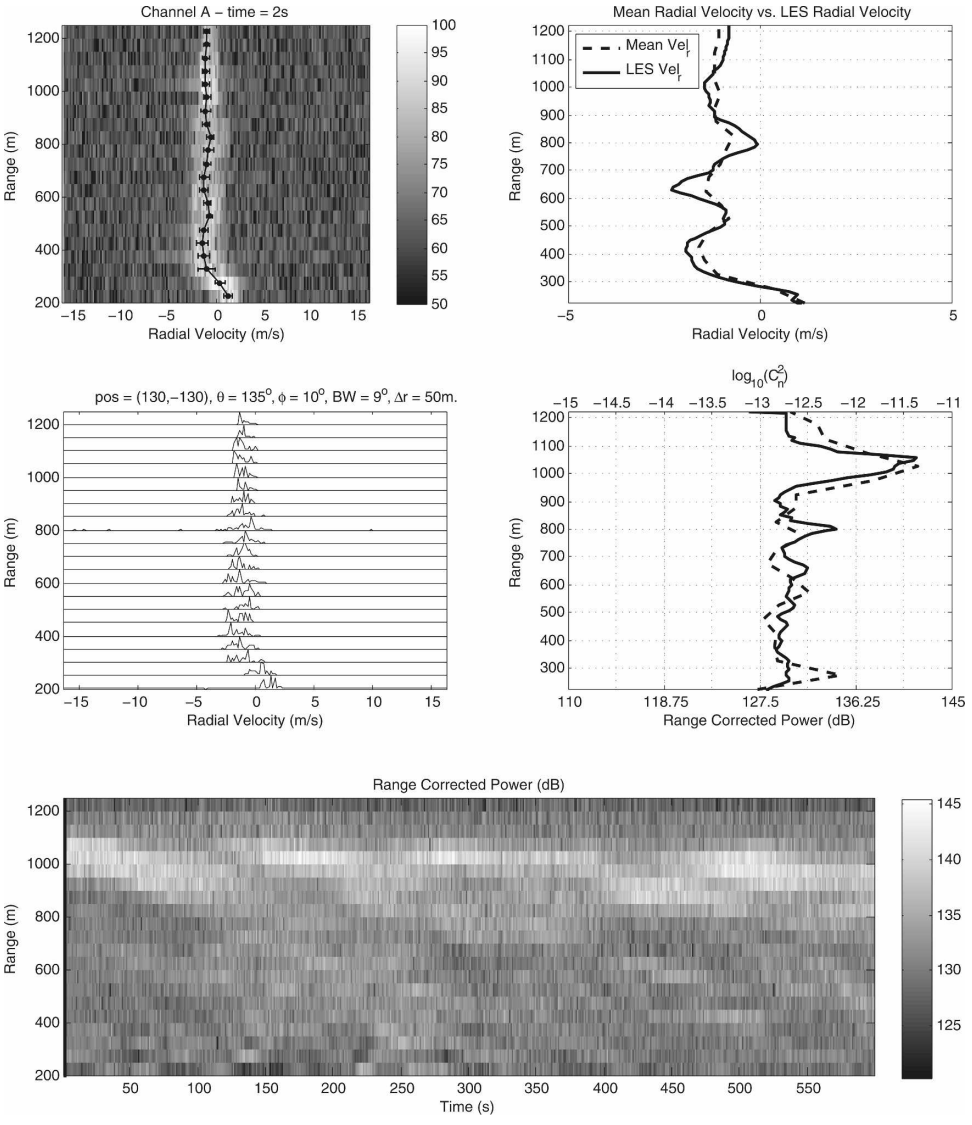

FIG. 5. Spectral analysis of the time series data. (top left) Intensity spectrum with additive white noise. The continuous line represents the mean radial velocity and the error bars represent the spectrum width. (top right) Comparison between the mean radial velocity estimated from the Doppler moments and the true radial velocity from the LES. (center left) Normalized stacked spectra. (center right) Comparison between the range-corrected power estimated form the virtual radar and the beam-weighted C_n^2 from the LES. The peak corresponds to the CBL top (inversion layer). (bottom) Range-corrected power (dB) estimated from the LES for the whole simulation period.

field components u, v, and w; the azimuth angle θ; and zenith angle ϕ as given by

$$v_r(\theta, \phi) = u \sin(\theta) \sin(\phi) + v \cos(\theta) \sin(\phi) + \cos(\phi). \tag{18}$$

When combining the five radars pointing at the same resolution volume, it is better to express them in the matrix form, as

$$\mathbf{v_r} = \mathbf{Au}, \tag{19}$$

where

$$\mathbf{A} = \begin{bmatrix} \sin(\theta_1)\sin(\phi_1) & \cos(\theta_1)\sin(\phi_1) & \cos(\phi_1) \\ \vdots & \vdots & \vdots \\ \sin(\theta_5)\sin(\phi_5) & \cos(\theta_5)\sin(\phi_5) & \cos(\phi_5) \end{bmatrix}, \tag{20}$$

$$\mathbf{u} = [uvw]^{\mathrm{T}}, \quad \text{and} \tag{21}$$

$$\mathbf{v_r} = [v_{r1}, \ldots, v_{r5}]^{\mathrm{T}}. \tag{22}$$

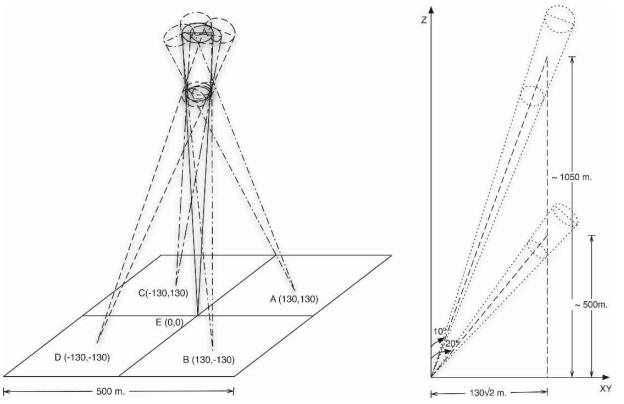

FIG. 6. Multiple radar experiment setup. The experiment was conducted using five radars pointing toward approximate the same resolution volume. (left) Location of the radars (four oblique and one vertical pointing beam) and (right) geometry of the radars pointing at two different heights (~500 and ~1050 m).

Using the system of equations presented above, the three-dimensional velocity vector **u** is estimated, in a least squares sense, using

$$\mathbf{u} = (\mathbf{A}\mathbf{A}^{\mathrm{T}})^{-1}\mathbf{A}^{\mathrm{T}}\mathbf{v}_{\mathbf{r}}. \tag{23}$$

Results of the analyses are presented in Figs. 9 and 10. The retrieved traces u, v, and w from the five radars are shown as continuous lines and the true values from the LES are depicted as dashed lines. At ~500 m, the retrieved values of horizontal wind components agree well with those from the LES. The retrieved and true values for the case of w, however, exhibit noticeable discrepancies. The converse is true for the measurements made at ~1050 m. Here, the vertical component of the wind shows better agreement between the retrieved and true values. Again, one expects some differences due to the disparate sampling volumes. We must also consider the effects of beam geometry, which factor into the solution of the three-dimensional wind vector. For example, the horizontal wind components

TABLE 3. Multiple radar experiment setup.

Radar	Position	Zenith angle (ϕ)	Azimuth angle (θ)
A	(130 m, 130 m)	20°	225°
B	(130 m, −130 m)	20°	315°
C	(−130 m, 130 m)	20°	135°
D	(−130 m, −130 m)	20°	45°
E	(0 m, 0 m)	0°	0°
A′	(130 m, 130 m)	10°	225°
B′	(130 m, −130 m)	10°	315°
C′	(−130 m, 130 m)	10°	135°
D′	(−130 m, −130 m)	10°	45°

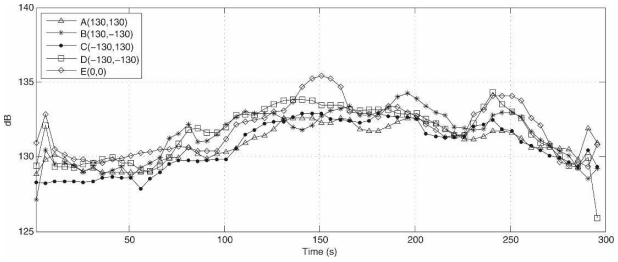

FIG. 7. Range-corrected power at ~500 m. All the radars show the same trend along the simulation. The resolution volumes for the five radars are almost the same.

are better represented for the sampling volume located at ~500 m. Correspondingly, the observed radial velocities contain a larger contribution from the vertical wind component for the case of the sampling volume at ~1050 m.

The simulation period is recognizably short (maximum 10 min); however, this represents a first stage in the validation of the radar-simulator code. Normally, the retrieved wind components for a UHF BLR are averaged over a sampling period of 30 min or more. We anticipate that better comparisons will be obtained when new LES data, corresponding to longer simulation runs, are available.

b. Frequency domain interferometry

At this point, we have only considered radar simulations with a range resolution of 50 m. Although commercially available BLRs are capable of achieving these resolutions, more typical values used for routine measurements are 100–300 m. The longer pulse widths result in better detectability of atmospheric signals. In Fig. 11 we show simulated radar data obtained with a 300-m resolution in range together with the C_n^2 field, which has a 10-m spacing. As can be observed, it is difficult to discriminate the top of the CBL or any other structures present within the 300-m resolution volume.

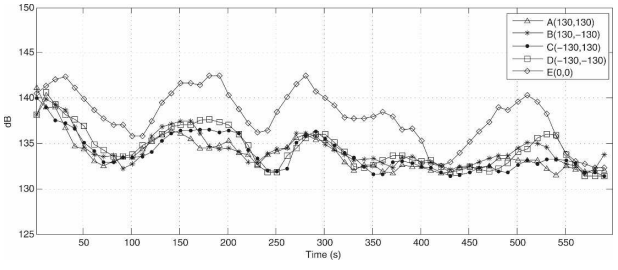

FIG. 8. Range-corrected power at ~1050 m. All the oblique radars show the same trend along the simulation. The bias observed by the vertical beam occurs because the resolution volume is not the same as it is for the oblique beam.

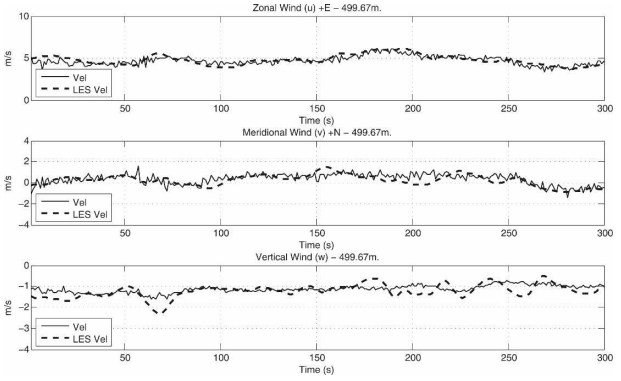

FIG. 9. Comparison between the velocities retrieved from the MRE at ~500 m directly from the LES.

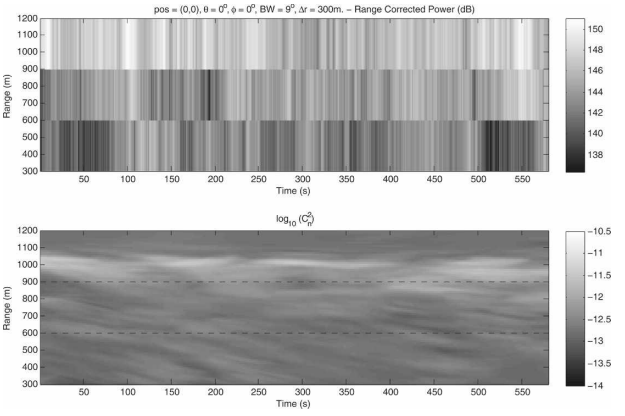

FIG. 11. (top) Range-corrected power retrieved from the BLR at a resolution of 300 m and (bottom) beam-weighted C_n^2.

Naturally, this will make accurate characterizations of the CBL problematic.

A technique called frequency domain interferometry was used by Kudeki and Stitt (1987, 1990), Palmer et al. (1990), and Chilson and Schmidt (1996) to help discriminate the height and thickness of localized scatterers within the resolution volume. The technique uses the phase difference of two signals separated in frequency by Δf to determine the position of a distinct and localized layer within the resolution volume. The layer is assumed to have a Gaussian shape. The FDI technique is typically implemented using a vertically pointing beam, although studies using oblique beams have been conducted (Palmer et al. 1992). The frequency difference should be chosen such that $\Delta f = f_h - f_l \leq 1/\tau$, which ensures that there is no ambiguity in the measured phase difference. However, even with this condition in place, it is only possible to estimate a relative layer position. The absolute position cannot be determined unless the initial transmitted phase is also known.

The FDI technique can only be used to locate a single layer within the resolution volume. If more than one layer is present, the technique fails. An extension of FDI called range imaging (RIM) was independently introduced by Palmer et al. (1999) and Luce et al. (2001) as a means of overcoming this limitation. In the RIM technique, several closely spaced carrier frequencies are used for transmission and reception. A constrained optimization method is invoked to image the reflectivity (and velocity) structure within the resolution volume.

Following the work of Kudeki and Stitt (1987), data from FDI experiments are analyzed by calculating the normalized cross-correlation function between the signals at different frequencies using

$$S_{hl} = \frac{\langle V_h V_l^* \rangle}{\left(\langle |V_h|^2 \rangle \langle |V_l|^2 \rangle\right)^{1/2}}, \tag{24}$$

where V_h and V_l are the complex time series of the signals obtained at the low and high frequencies, respectively. The angle brackets $\langle\rangle$ represent the expected value operator. The magnitude (coherence) and phase of S_{hl} is given by

$$|S_{hl}| = \exp(-2\Delta k^2 \sigma_l^2), \quad \text{and} \tag{25}$$

$$\phi = 2\Delta k \langle r \rangle, \tag{26}$$

where Δk is the difference in the wavenumbers between the two frequencies ($\Delta k = 2\pi\Delta f/c$) and c is the speed of light. The relative layer location and thickness are given by $\langle r \rangle$ and $2\sigma_l$, respectively.

For the present experiment, two closely spaced frequencies were selected (915.0 and 915.5 MHz) to optimize the difference to the chosen range resolution of the radar (300 m). After applying FDI, and using Eqs. (25) and (26), the relative position and layer thickness—$\langle r(v_r) \rangle$ and $2\sigma_l(v_r)$, respectively—are determined;

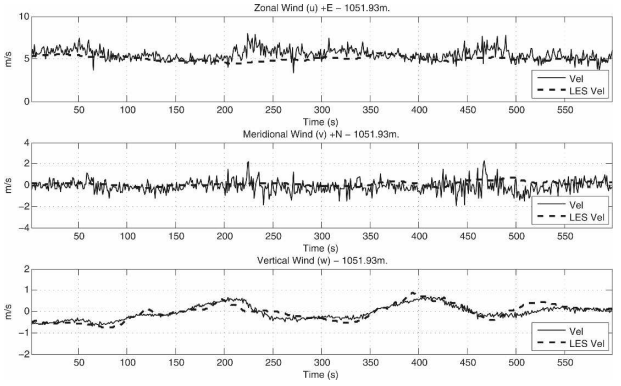

FIG. 10. Same as in Fig. 9, but for ~1050 m.

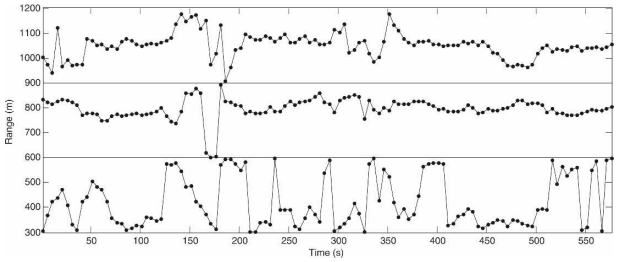

FIG. 12. Relative position of the layer within the range resolution. The uncertainties after comparing with the weighted C_n^2 occur because the random initial phases for the two frequencies are not taken into account when computing the phase of the cross-correlation function.

they are presented in Figs. 12 and 13. The former shows the relative position of the layer within the resolution volume, and the latter presents the thickness (0–300 m) of the layer within the resolution volume.

As mentioned before, the FDI technique allows the discrimination of a single layer within the resolution volume. When analyzing the range 300–600 m, a nondefined layer was found. Even when the thickness of the layer fluctuates around 150 m, the position randomly oscillates along the range, confirming that no significant layer was present. For the case of 600–900 m, a layer with a thickness of approximately 100 m is observed around 850 m, which agrees with the beam-weighted C_n^2 presented in Fig. 11, even when it has low values of C_n^2. Finally, when examining the 900–1200-m range, another clear layer can be depicted at approximately 1050 m, with a thickness of approximately 150 m, which clearly agrees with the range-weighted C_n^2.

Some differences have been observed in the estimates of the position of the layer. These can be attributed to the fact that the radar simulator uses a random initial phase, which is not taken into account when the cross-correlation phase is calculated (calibration effect). The layer thickness estimates are usually wider than the true layer. Better estimates of the layer thickness are expected once RIM has been implemented on the radar simulator, which is planned as a future refinement.

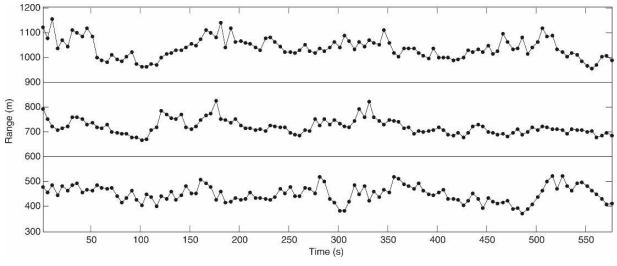

FIG. 13. Layer thickness estimates within the resolution volume. The thickness range per gate oscillates between 0 and 300 m.

5. Conclusions

Based on the work of MSW99, a refined LES-based radar simulator suitable for studies of the convective boundary layer has been presented. The simulator is capable of producing realistic time series data for idealized CBLs and has sufficient flexibility to allow for a wide range of virtual radar experiments. For example, one can select the beam direction, beamwidth, and pulse width, and simultaneously deploy a large number of virtual radars. The radar simulator is also designed to accommodate multiple frequency applications.

The primary differences between the virtual BLR presented here and the one developed by MSW99 can be summarized as follows:

1) the present virtual BLR can accommodate multiple beams (vertical and off-vertical), which is made possible through the calculation of oblique C_n^2 at arbitrary angles;
2) velocity and C_n^2 values are interpolated for each time step of the virtual BLR;
3) noise has been generated and injected into the time series data; and
4) a multiple frequency operation has been simulated.

Initial tests have been completed and the radar simulator outputs have been compared with the original LES-generated fields on which the simulator is based. Retrieved range-corrected power estimates are consistent with corresponding values calculated for C_n^2. Furthermore, analysis of the simulated radar time series data shows that they have a spectral content consistent with the u, v, and w fields from the LES. FDI experiments demonstrated that it is possible to accurately retrieve the relative position and thickness of a single layer within the range resolution volume from the generated time series data. An improvement to this technique is called range imaging (RIM; Palmer et al. 1999; Luce et al. 2001; Chilson et al. 2003), which uses more than two frequencies to estimate the characteristics of more than one layer. It is planned to incorporate RIM into the radar simulator. One of the fundamental motivations for developing the radar simulator is to examine the applicability of various methods used to extract turbulence characteristics of the CBL from actual BLR data. In addition, it is intended to use these characterizations to validate output from the LES model runs. To accomplish these goals, a two-pronged approach is planned, exploiting data from both the radar simulator and radar field studies. In either case, the fundamental

problem—the extraction of high-resolution turbulence intensity measurements from radar data (e.g., Gage and Balsley 1984; Hocking 1983, 1985), whether actual or synthetic—remains.

Unfortunately, there are no direct methods or simple algorithms to relate turbulence parameters to radar observations. One commonly used practice relies on the relationship between radar reflectivity η and the structure function parameter of the refractive index C_n^2. Given the nonstationarity and inhomogeneity of turbulence in the CBL, it is unlikely that the resolution volume ever fulfills the assumption that it is filled on the scale of a typical resolution volume. With the high vertical resolution measurements made possible with RIM, however, the filled volume assumption has more validity because the range weighting function (range resolution) is much smaller than with standard processing. This method of estimating turbulence intensity requires estimates of the radar reflectivity, which is only possible with a power-calibrated radar. However, even if the exact proportionality coefficient is not known, it is still possible to use this method to study the temporal and spatial variations of relative differences in the C_n^2 field.

A second method of estimating turbulence intensity is through remotely sensed velocity variations (e.g., Brewster and Zrnić 1986). The Doppler spectrum is an approximation of a power-weighted distribution of radial velocities within the resolution volume of the radar. The standard deviation of the Doppler spectrum (i.e., the spectrum width σ_v) can be related to the turbulence energy dissipation rate ε (Hocking 1985). The measurement of the width of the Doppler spectrum can be problematic in that there are several phenomena that tend to bias it to larger values, such as wind shear and finite beamwidth effects (Nastrom 1997; White 1997; White et al. 1999). Given a known beam pattern of the radar and standard Doppler beam swinging measurements, however, it is possible to minimize these effects and estimate the velocity variation due to turbulence (Cohn 1995; White 1997; White et al. 1999).

Acknowledgments. Support for this work was provided by the National Science Foundation under Grant 0553345.

REFERENCES

Angevine, W. M., 1999: Entrainment results including advection and case studies from the Flatland boundary layer experiments. *J. Geophys. Res.,* **104,** 30 947–30 963.

——, A. B. White, and S. K. Avery, 1994: Boundary-layer depth and entrainment zone characterization with a boundary-layer profiler. *Bound.-Layer Meteor.,* **68,** 375–385.

Balsley, B. B., and K. Gage, 1982: On the use of radars for operational wind profiling. *Bull. Amer. Meteor. Soc.,* **63,** 1009–1018.

Bean, B. R., and E. J. Dutton, 1966: *Radio Meteorology*. *National Bureau of Standards Monogr.,* No. 92, U.S. Government Printing Office, 435 pp.

Brewster, K. A., and D. S. Zrnić, 1986: Comparison of eddy dissipation rates from spatial spectra of Doppler velocities and Doppler spectrum widths. *J. Atmos. Oceanic Technol.,* **3,** 440–452.

Cheong, B. L., M. W. Hoffman, and R. D. Palmer, 2004: Efficient atmospheric simulation for high-resolution radar imaging applications. *J. Atmos. Oceanic Technol.,* **21,** 374–378.

Chilson, P. B., 2004: The retrieval and validation of Doppler velocity estimates from range imaging. *J. Atmos. Oceanic Technol.,* **21,** 1033–1043.

——, and G. Schmidt, 1996: Implementation of frequency domain interferometry at the SOUSY VHF radar: First results. *Radio Sci.,* **31,** 263–272.

——, T.-Y. Yu, R. G. Strauch, A. P. Muschinski, and R. D. Palmer, 2003: Implementation and validation of range imaging on a UHF radar wind profiler. *J. Atmos. Oceanic Technol.,* **20,** 987–996.

Cohn, S. A., 1995: Radar measurements of turbulent eddy dissipation rate in the troposphere: A comparison of techniques. *J. Atmos. Oceanic Technol.,* **12,** 85–95.

——, and W. M. Angevine, 2000: Boundary level height and entrainment zone thickness measured by lidars and wind-profiling radars. *J. Appl. Meteor.,* **39,** 1233–1247.

Conzemius, R. J., and E. Fedorovich, 2006: Dynamics of sheared convective boundary layer entrainment. Part I: Meteorological background and large-eddy simulations. *J. Atmos. Sci.,* **63,** 1151–1178.

Dabberdt, W. F., G. L. Frederick, R. M. Hardesty, W. C. Lee, and K. Underwood, 2004: Advances in meteorological instrumentation for air quality and emergency response. *Meteor. Atmos. Phys.,* **87,** 57–88.

Deardorff, J. W., 1972: Numerical investigation of neutral and unstable planetary boundary layers. *J. Atmos. Sci.,* **29,** 91–115.

Doviak, R. J., and D. S. Zrnić, 1993: *Doppler Radar and Weather Observations.* 2nd ed. Academic Press, 562 pp.

Eaton, F. D., S. A. McLaughlin, and J. R. Hines, 1995: A new frequency-modulated continuous wave radar for studying planetary boundary layer morphology. *Radio Sci.,* **30,** 75–88.

Ecklund, W. L., K. S. Gage, and C. R. Williams, 1995: Tropical precipitation studies using a 915-MHz wind profiler. *Radio Sci.,* **30,** 1055–1064.

Fedorovich, E., F. T. M. Nieuwstadt, and R. Kaiser, 2001: Numerical and laboratory study of a horizontally evolving convective boundary layer. Part I: Transition regimes and development of the mixed layer. *J. Atmos. Sci.,* **58,** 70–86.

——, and Coauthors, 2004a: Entrainment into sheared convective boundary layers as predicted by different large-eddy simulation codes. Preprints, *16th Symp. on Boundary Layers and Turbulence,* Portland, ME, Amer. Meteor. Soc., P4.7. [Available online at http://ams.confex.com/ams/pdfpapers/78656.pdf.]

——, R. Conzemius, and D. Mironov, 2004b: Convective entrainment into a shear-free linearly stratified atmosphere: Bulk models reevaluated through large-eddy simulations. *J. Atmos. Sci.,* **61,** 281–295.

Gage, K. S., and B. B. Balsley, 1984: MST radar studies of wind

and turbulence in the middle atmosphere. *J. Atmos. Terr. Phys.,* **46,** 739–753.

——, C. R. Williams, and W. L. Ecklund, 1994: UHF wind profilers: A new tool for diagnosing and classifying tropical convective cloud systems. *Bull. Amer. Meteor. Soc.,* **75,** 2289–2294.

Grimsdell, A. W., and W. M. Angevine, 2002: Observation of the afternoon transition of the convective boundary layer. *J. Appl. Meteor.,* **41,** 3–11.

Hildebrand, P. H., and R. S. Sekhon, 1974: Objective determination of the noise level in Doppler spectra. *J. Appl. Meteor.,* **13,** 808–811.

Hocking, W. K., 1983: On the extraction of atmospheric turbulence parameters from radar backscatter Doppler spectra. Part I: Theory. *J. Atmos. Terr. Phys.,* **45,** 89–102.

——, 1985: Measurement of turbulent eddy dissipation rates in the middle atmosphere by radar techniques: A review. *Radio Sci.,* **20,** 1403–1422.

Holdsworth, D. A., and I. M. Reid, 1995: A simple model of atmospheric radar backscatter: Description and application to the full correlation analysis of spaced antenna data. *Radio Sci.,* **30,** 1263–1280.

Holton, J. R., 2004: *An Introduction to Dynamic Meteorology.* 4th ed. Academic Press, 535 pp.

Holtslag, A. A. M., and P. G. Duynkerke, Eds., 1998: *Clear and Cloudy Boundary Layers.* Royal Netherlands Academy of Arts and Sciences, 372 pp.

Khanna, S., and J. G. Brasseur, 1998: Three-dimensional buoyancy- and shear-induced local structure of the atmospheric boundary layer. *J. Atmos. Sci.,* **55,** 710–743.

Kudeki, E., and G. R. Stitt, 1987: Frequency domain interferometry: A high-resolution radar technique for studies of atmospheric turbulence. *Geophys. Res. Lett.,* **14,** 198–201.

——, and ——, 1990: Frequency domain interferometry studies of mesospheric layers at Jicamarca. *Radio Sci.,* **25,** 575–590.

Luce, H., M. Yamamoto, S. Fukao, D. Helal, and M. Crochet, 2001: A frequency domain radar interferometric imaging (FII) technique based on high-resolution methods. *J. Atmos. Solar-Terr. Phys.,* **63,** 221–234.

Mason, P. J., 1989: Large-eddy simulation of the convective atmospheric boundary layer. *J. Atmos. Sci.,* **46,** 1492–1516.

Moeng, C.-H., 1984: A large-eddy-simulation model for the study of planetary boundary layer turbulence. *J. Atmos. Sci.,* **41,** 2052–2062.

——, and P. P. Sullivan, 1994: A comparison of shear- and buoyancy-driven planetary boundary layer flows. *J. Atmos. Sci.,* **51,** 999–1022.

Muschinski, A. P., P. P. Sullivan, D. B. Wuertz, R. J. Hill, S. A. Cohn, D. H. Lenschow, and R. J. Doviak, 1999: First synthesis of wind-profiler signal on the basis of large-eddy simulation data. *Radio Sci.,* **34,** 1437–1459.

Nastrom, G. D., 1997: Doppler radar spectral width broadening due to beamwidth and wind shear. *Ann. Geophys.,* **15,** 786–796.

Nieuwstadt, F. T. M., 1990: Direct and large-eddy simulation of free convection. *Proc. Ninth Int. Heat Transfer Conf.,* Jerusalem, Israel, American Society of Mechanical Engineers, 37–47.

Ottersten, H., 1969: Mean vertical gradient of potential refractive index in turbulent mixing and radar detection of CAT. *Radio Sci.,* **4,** 1247–1249.

Palmer, R. D., R. F. Woodman, S. Fukao, M. F. Larsen, M. Yamamoto, T. Tsuda, and S. Kato, 1990: Frequency domain interferometry observations of tropo/stratospheric scattering layers using the MU radar: Description and first results. *Geophys. Res. Lett.,* **17,** 2189–2192.

——, S. Fukao, M. F. Larsen, M. Yamamoto, T. Tsuda, and S. Kato, 1992: Oblique frequency domain interferometry measurements using the middle and upper atmosphere radar. *Radio Sci.,* **27,** 713–720.

——, T.-Y. Yu, and P. B. Chilson, 1999: Range imaging using frequency diversity. *Radio Sci.,* **34,** 1485–1496.

Rogers, R. R., W. L. Ecklund, D. A. Carter, K. S. Gage, and S. A. Ethier, 1993: Research applications of a boundary-layer wind profiler. *Bull. Amer. Meteor. Soc.,* **74,** 567–580.

Schmidt, H., and U. Schumann, 1989: Coherent structure of the convective boundary layer derived from large-eddy simulations. *J. Fluid Mech.,* **200,** 511–562.

Sheppard, E. L., and M. F. Larsen, 1992: Analysis of model simulations of spaced antenna/radar interferometer measurements. *Radio Sci.,* **27,** 759–768.

Sorbjan, Z., 1996: Effects caused by varying the strength of the capping inversion based on a large-eddy simulation model of the shear-free convective boundary layer. *J. Atmos. Sci.,* **53,** 2015–2024.

——, 2004: Large-eddy simulations of the baroclinic mixed layer. *Bound.-Layer Meteor.,* **112,** 57–80.

Stevens, B., and D. H. Lenschow, 2001: Observations, experiments, and large-eddy simulation. *Bull. Amer. Meteor. Soc.,* **82,** 283–294.

Sullivan, P., C.-H. Moeng, B. Stevens, D. H. Lenschow, and S. D. Mayor, 1998: Structure of the entrainment zone capping the convective atmospheric boundary layer. *J. Atmos. Sci.,* **55,** 3042–3064.

Tatarskii, V. I., 1961: *Wave Propagation in a Turbulent Medium.* McGraw-Hill, 285 pp.

Taylor, G. I., 1938: The spectrum turbulence. *Proc. Roy. Soc. London,* **164A,** 476–490.

VanZanten, M. C., P. G. Duynkerke, and J. W. M. Cuijpers, 1999: Entrainment parameterization in convective boundary layers. *J. Atmos. Sci.,* **56,** 813–828.

White, A. B., 1997: Radar remote sensing of scalar and velocity micro turbulence in the convective boundary layer. NOAA Tech. Memo. ERL ETL-276, Environmental Technology Laboratory, 127 pp.

——, R. J. Lataitis, and R. S. Lawrence, 1999: Space and time filtering of remotely sensed velocity turbulence. *J. Atmos. Oceanic Technol.,* **16,** 1967–1972.

Wilczak, J. M., E. E. Gossard, W. D. Neff, and W. L. Eberhard, 1996: Ground-based remote sensing of the atmospheric boundary layer: 25 years of progress. *Bound.-Layer Meteor.,* **78,** 321–349.

Wyngaard, J. C., 1998: Experiment, numerical modeling, numerical simulation, and their roles in the study of convection. *Buoyant Convection in Geophysical Flows,* E. J. Plate et al., Eds., Kluwer Academic, 239–252.

Yu, T.-Y., 2000: Radar studies of the atmosphere using spatial and frequency diversity. Ph.D. thesis, University of Nebraska, 224 pp.

Zilitinkevich, S. S., 1991: *Turbulent Penetrative Convection.* Avebury Technical, 179 pp.